On the proper interpretation of ionospheric conductance estimated through satellite photometry

Joshua Semeter and Richard Doe
SRI International, Menlo Park, California, USA

Received 8 October 2001; revised 10 January 2002; accepted 7 March 2002; published 23 August 2002.

[1] As a consequence of the electron continuity equation, ionospheric conductance derived from photometric measurements of the aurora represents a root-mean-square over the field of view and exposure time of the photometer, and not a true average. The magnitude of the discrepancy between these estimates depends on the statistical variance of the electron density within the sampling window and is therefore strongly dependent on both the resolution of the sensor and the activity of the aurora. We use high-resolution optical and incoherent scatter radar measurements to quantify the relationship among the instantaneous ("true") conductance, the average conductance, and the photometrically derived conductance during an auroral substorm over Sondrestrom, Greenland. For a 36 s exposure time (typical for the ultraviolet imager (UVI) sensor on the Polar satellite), we show that the photometric estimate can be biased from the average value by 40% for Hall and 20% for Pedersen; the mean, in turn, can misrepresent the true conductance by more than 150% for Hall and 100% for Pedersen, owing to undersampling small-scale variability. We develop two schemes for correcting (in the former case) and understanding (in the latter case) these effects using conjunctive ground-based diagnostics. *INDEX TERMS:* 2455 Ionosphere: Particle precipitation; 2794 Magnetospheric Physics: Instruments and techniques; 2407 Ionosphere: Auroral ionosphere (2704); 2716 Magnetospheric Physics: Energetic particles, precipitating; 2736 Magnetospheric Physics: Magnetosphere/ionosphere interactions; *KEYWORDS:* incoherent scatter radar, ionospheric conductance, UV imaging, auroral precipitation

1. Introduction

[2] Spectral photometry of the aurora has long been used to infer the kinetic energy flux of incident electrons [*Rees and Luckey*, 1974; *Strickland et al.*, 1989] and the associated increase in ionospheric conductance [i.e., *Vickrey et al.*, 1981; *Wallis and Budzinski*, 1981; *Spiro et al.*, 1982; *Germany et al.*, 1994]. A linear relationship between luminosity and energy flux arises from the proportionality between energy deposition rate and photon production rate for several wavelength regimes. In such cases, energy flux derived from a photometric measurement can be accurately interpreted as the mean value over the spatial and temporal resolution of the sensor.

[3] The connection between luminosity and conductance, however, is through a continuity rule that relates volume production rate to plasma density in a nonlinear way. This step introduces a bias into estimated ionospheric parameters whenever the temporal and spatial scales of auroral variability are small compared to the resolution of the sensor – a limitation which affects all satellite-based imaging systems (e.g., those on ISIS, AE, DE, Polar, IMAGE, and TIMED); the Polar ultraviolet imager (UVI) sensor, for example, is typically operated with an exposure time of 36 s and an E region spatial resolution of $\sim$40 kilometers [*Torr et al.*, 1995]. The discrete aurora, on the other hand, can form in spatial scales of <1 km and on time scales of <1 s during active periods.

[4] The purpose of this work is to quantify the effects of undersampling on photometrically derived conductance, and to develop a framework for treating these effects using higher-resolution diagnostics. Both the magnitude of the errors and the efficacy of the proposed solutions are evaluated using high-resolution ground-based measurements during an auroral substorm over the Sondrestrom, Greenland, incoherent scatter (IS) radar facility. Our approach involves degrading these measurements to the spatial-temporal resolution of a space-based imaging photometer. We use the Polar UVI sensor as a reference, but the results are relevant to any inference of ionospheric density and conductance by optical means. The proper treatment of sampling effects is relevant to efforts that seek to assimilate ground-based and space-based measurements into a coherent picture of magnetosphere–ionosphere coupling [e.g., *Kamide et al.*, 1981; *Richmond and Kamide*, 1988].

2. Estimating Conductance From Luminosity

[5] The estimation of ionospheric conductance from photometric measurements rests on the premise that the production rate of electron-ion pairs q as a function of field-aligned altitude z can be determined from a discrete set of brightness measurements $\epsilon = [\epsilon_1, \epsilon_2, \ldots]$. In the case of Polar UVI, two measurements are used – namely, the Lyman-Birge-Hopfield-long (LBHL) and -short (LBHS) bands of

0148-0227/02/2001JA009101$09.00

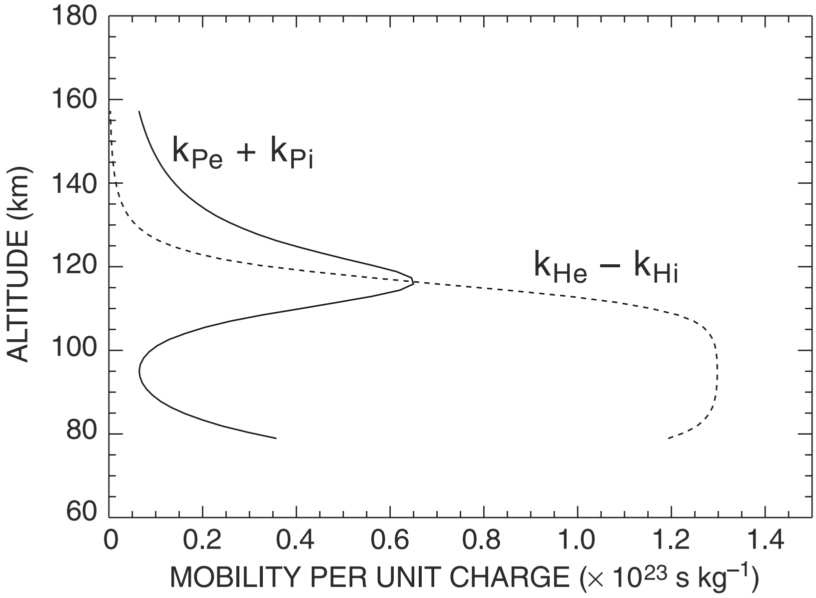

Figure 1. Total Pedersen and Hall mobilities as a function of altitude for a typical high-latitude wintertime ionosphere for electrons.

N_2 [*Germany et al.*, 1994; *Torr et al.*, 1995; *Doe et al.*, 1997]. Referring to these measurements as ϵ_L and ϵ_S, respectively, this inverse problem can be stated canonically:

$$q(z) = f(\epsilon_L, \epsilon_S). \tag{1}$$

The problem is ill-posed because it seeks a continuous function from discrete measurements. In practice, spectral brightness is first used to parameterize the incident electron energy spectrum, from which q is calculated using a numerical model of electron transport and energy deposition [*Rees*, 1963; *Lummerzheim and Lilensten*, 1994; *Strickland et al.*, 1989].

[6] For the LBHL emission, photon production rate is proportional to ion production rate such that

$$\epsilon_L = K \int_0^\infty q \partial z, \tag{2}$$

where K is a calibration constant. By comparison with equation (1), we see that evaluating f is equivalent to inverting equation (2). In this view, the additional measurement ϵ_S serves to constrain the nonunique inverse problem.

[7] To relate q to conductivity, a continuity rule is required. In the auroral E region, electron density is governed by particle production and chemical loss, with transport and diffusion negligible, such that

$$\frac{\partial N}{\partial t} = q - \alpha N^2, \tag{3}$$

where N is electron density, and α is an effective recombination coefficient acting on an equal number of ions and electrons. A functional form for α has been proposed by *Vickrey et al.* [1982] as a reasonable fit to published results,

$$\alpha = 2.5 \times 10^{-6} \exp(-z/51.2) \left[\mathrm{cm}^3/\mathrm{s}\right], \tag{4}$$

with z in kilometers.

[8] In the analysis of satellite imagery, steady state is assumed such that continuity is expressed as

$$q = \alpha N^2. \tag{5}$$

This approximation is rarely justified on physical grounds but, rather, the long sampling period required to obtain ϵ precludes detection of non-steady state conditions. We will demonstrate that violations of the steady state assumption are an important consideration for properly interpreting derived ionospheric parameters during auroral substorms.

[9] Next, the Hall and Pedersen conductivities can be expressed, respectively, as

$$\sigma_H = Ne^2(k_{He} - k_{Hi}) \tag{6}$$

$$\sigma_P = Ne^2(k_{Pe} + k_{Pi}) \tag{7}$$

where k_{He} and k_{Hi} are the altitude-dependent Hall mobilities per unit charge for electrons and ions, respectively, and k_{Pe} and k_{Pi} are the Pedersen mobilities for electrons and ions, respectively, given by

$$k_{He,i} = \frac{1}{Be} \frac{\omega_{e,i}^2}{\nu_{e,i}^2 + \omega_{e,i}^2} \tag{8}$$

$$k_{Pe,i} = \frac{1}{Be} \frac{\nu_{e,i}\omega_{e,i}}{\nu_{e,i}^2 + \omega_{e,i}^2} \tag{9}$$

[*Rishbeth and Garriott*, 1969] where ω is the gyrofrequency, ν is the collision frequency, and e is the charge of an electron. Although equations (8) and (9) differ from the conventional expressions for mobility, defined as a ratio of velocity to electric field, they have the advantage of being valid for both electrodynamic and mechanical forces.

[10] Figure 1 gives a plot of the right-hand terms of equations (8) and (9) versus altitude for typical high-latitude wintertime conditions. These curves can be interpreted

weighting factors that relate electron density to conductivity. Between 85 and 105 km, ($k_{He} - k_{Hi}$) is nearly constant; electron density is proportional to Hall conductance in this range. By comparison, the sensitivity of Pedersen conductance to electron density is strongly peaked at 120 km.

[11] Integrating equations (6) and (7) over z gives the conductances,

$$\Sigma_H = \int_0^\infty e^2 (k_{He} - k_{Hi})\, N\, \partial z, \tag{10}$$

$$\Sigma_P = \int_0^\infty e^2 (k_{Pe} + k_{Pi})\, N\, \partial z. \tag{11}$$

It is insightful to compare this result with the expression for LBHL luminosity ϵ_L derived by combining equations (2) and (5):

$$\epsilon_L = \int_0^\infty K\alpha\, N^2\, \partial z. \tag{12}$$

Equations (10)–(12) show clearly that conductance is not proportional to luminosity, nor is it proportional to $\int_0^\infty N \partial z$. To derive conductance photometrically, one must derive the full altitude distribution of N.

[12] Equations (1) through (11) constitute a closed set of relations by which conductivity is estimated from auroral photometry. A more detailed treatment has been presented most recently by *Germany et al.* [1994]. For the purposes of this work, we assume that our model is exact; that is, Σ_H and Σ_P can be exactly derived from ϵ. We focus, instead, on the resolution limitations of the optical measurement and how these effects propagate through the calculation.

3. Connection With Sensor Resolution

[13] A measurement of auroral luminosity represents an average over the spatial and temporal resolution of the sensor. Consider, first, the time dimension. By equation (2), a photometric measurement at time t with exposure period T is equivalent to a measurement of the average production rate over T; that is,

$$\langle q(t) \rangle \equiv \frac{1}{T} \int_{-T/2}^{T/2} q(t - \tau) \partial \tau, \tag{13}$$

where the brackets indicate an average. Combining equation (13) with equation (5) and solving for N gives

$$\widetilde{\langle N(t) \rangle} = \left[\frac{1}{T} \int_{-T/2}^{T/2} N^2 (t - \tau) \partial \tau \right]^{\frac{1}{2}}, \tag{14}$$

where the $\widetilde{\langle N \rangle} = \sqrt{\langle N^2 \rangle}$ is the photometrically derived electron density estimate used to derive conductance. Equation (14) is the root-mean-square (RMS) value over interval T. The true average is simply

$$\langle N(t) \rangle = \frac{1}{T} \int_{-T/2}^{T/2} N(t - \tau) \partial \tau. \tag{15}$$

If we are interested in the average conductance over T, equation (15) should be used, but in satellite photometry, equation (14) is implicitly used. The derived density $\langle N \rangle$ will always be greater than or equal to the true average $\langle N \rangle$. The two are equal only if N is constant over T; otherwise, there will be a systematic overestimation of photometrically derived density and conductance.

[14] An analogous bias is introduced by spatial variability. Without loss of generality, we may rewrite equation (13) as

$$\langle q(\mathbf{r}, t) \rangle = \frac{1}{AT} \int_{\boldsymbol{S}} \int_{-T/2}^{T/2} q(\mathbf{r} - \gamma, t - \tau) \partial \tau \partial \gamma, \tag{16}$$

where $\boldsymbol{r}$ is the spatial coordinate and the spatial integration is over $\boldsymbol{S}$, the E region surface subtended by the pixel, with A the pixel's projected area. Although spatial and temporal variability in the auroral source may have very distinct consequences for magnetosphere–ionosphere coupling, the effects propagate identically in the mathematical derivation of conductance.

[15] We now wish to quantify the significance of this bias for a given pixel size and exposure time. This requires that we sample N at sufficiently high resolution so as to approximate an instantaneous measurement. From these measurements, we may estimate $\langle N \rangle$ and $\langle N \rangle$ in equations (14) and (15) by discrete integration over a typical Polar UVI sampling period. Substituting these results into equations (10) and (11) will allow us to compare the "true" conductance Σ with the average conductance $\langle \Sigma \rangle$, and the simulated photometrically derived conductance $\langle \Sigma \rangle$.

4. Experiment Description

[16] An experiment was conducted in February–March, 2001, with the Sondrestrom facility instrumentation to investigate E region variability during an auroral substorm at the highest possible time and spatial resolution. The IS radar operated with a 5 baud Barker coded pulse scheme, providing samples of electron density from 80 to 160 km in the magnetic zenith at 1.5 km altitude resolution and 1.2 s time resolution. This sampling period is small compared to the 36 s exposure time of the Polar UVI sensor and is of the same order as the typical e-folding time of the E region plasma density to an auroral input (typically a few seconds) [*Brekke*, 1997].

[17] For high-resolution measurements of ϵ, a narrow-field intensified CCD camera provided images over a $12° \times 15°$ field of view in the magnetic zenith at 40 ms time resolution and 300 m spatial resolution. This instrument used an edge filter to pass only wavelengths longer than 640 nm, thereby rejecting the forbidden transitions of atomic oxygen at 630.0 and 557.7 nm. This instrument allowed us to measure variability in the auroral source on time scales limited only by the detector sensitivity, not by radiative lifetimes of the emitting species. In this wavelength regime, the discrete aurora is dominated by the First Positive band system of N_2 whose intensity is approximately proportional to the integrated ion production rate [*Semeter et al.*, 2001] – similar to LBHL. The measured luminosity in the magnetic zenith can, thus, be considered a high-resolution proxy for ϵ_L.

5. Results

[18] Figure 2a gives a plot of raw electron density in the magnetic zenith recorded during a 10 min period of auroral

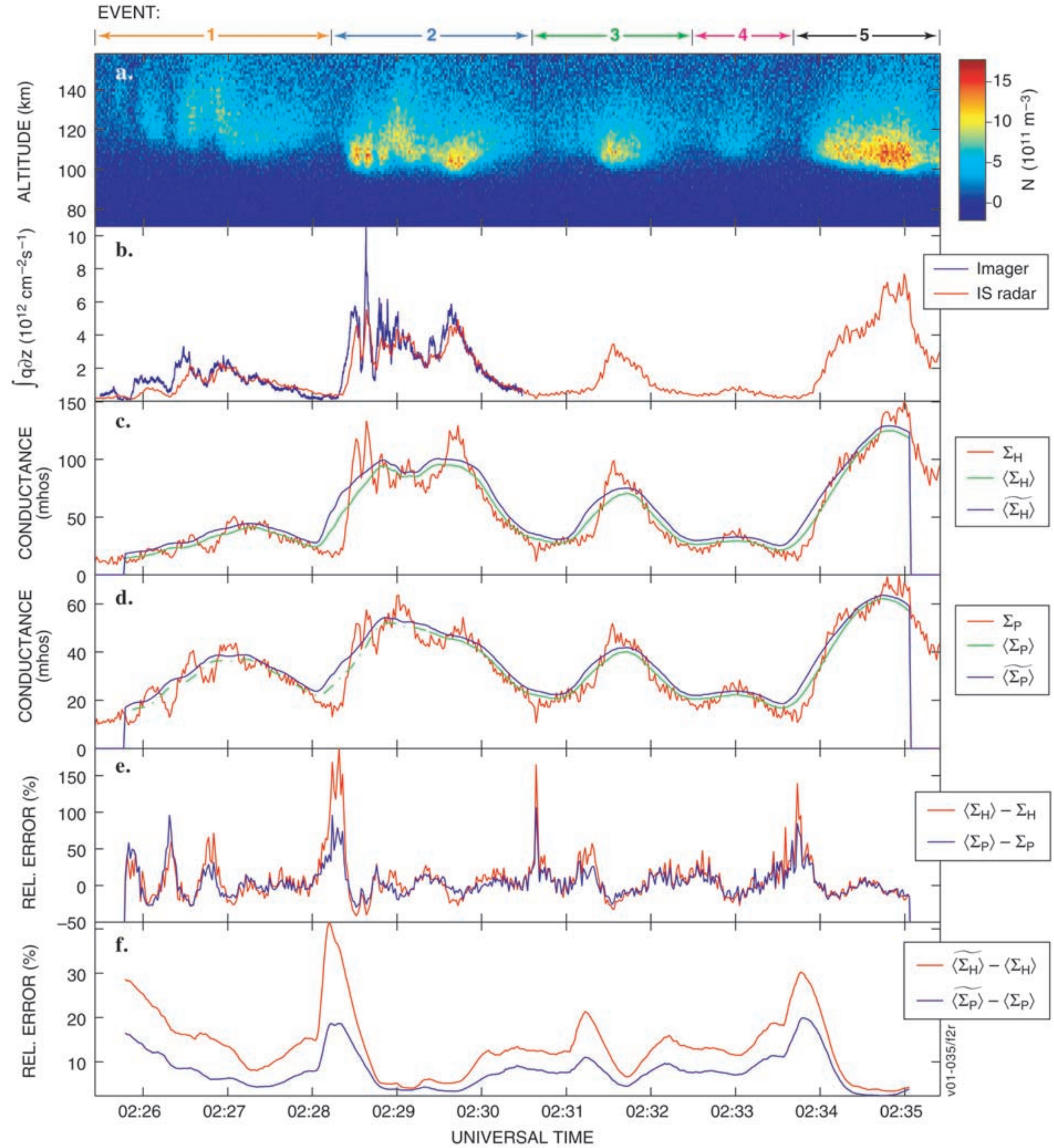

Figure 2. Electron densities and conductances derived from Sondrestrom incoherent scatter radar measurements on February 17, 2001, 02:25 to 02:35 UT: a. Electron density (1.5 km × 1.2 s samples). b. Comparison of height-integrated production of electron-ion pairs calculated via IS radar and simulated from ground-based luminosity. c. Comparison of Hall conductance calculated from electron densities in panel at full resolution (red), smoothed over a 36 s sliding window (green), and from the 36 s RMS value (simulating the photometric estimate) (blue). d. Same as c, but for Pederson conductance. e. Relative error between true and average conductance. f. Relative error between average and photometrically derived conductance.

activity on February 17, 2001. For analysis purposes, the *E* region enhancements have been organized into five separate events identified by the color-coded bars along the top.

[19] This period shows a considerable range of auroral variability, with density enhancements ranging from 1×10^{11} to 2×10^{12} m^{-3} over altitudes ranging from 80 to 150 km. To appreciate the degree of spatial and temporal variability in the corresponding optical aurora, Figure 3 shows samples from the video sequence for Event 2 at 2 s intervals. Universal time is shown in the top of each image,

and the projected 1 km spot size of the IS radar beam is given by the circle. Note that this field of view (21 × 26 km) is similar in size to a single pixel on the Polar UVI imager at perigee, and the sequence shown is similar in length to a typical UVI exposure time. Figure 3, thus, reveals the detail that would be filtered out in satellite-based imagery of this event.

[20] Figure 2b compares the optical luminosity in the magnetic zenith extracted from the video sequence (blue curve) with height-integrated electron production rate calculated for the radar profiles under the steady state model of equation (12) (red curve). (Optical data were only available before 0230 UT.) The calibration constant K was chosen to best match the optical measurements to the radar-derived production rates during the 02:29 to 02:30 UT interval – a interval of slowly varying luminosity where $\partial N/\partial t$ was small compared to the rate of plasma recombination. The two estimates of production rate agree quite well under this simple model, but some disagreement is evident. Some of the discrepancy is caused by inaccuracies in the *Vickrey et al.* [1982] parameterization of α. Another effect appears during intervals of high variability, where the radar estimate of production rate lags the luminosity (e.g., at 0225:30 UT and 0228 UT). This indicates a violation of the steady state approximation applied in the analysis, an important consideration that we will return to later.

[21] We now wish to quantify the relationship among Σ, $\langle\Sigma\rangle$ and $\langle\Sigma\rangle$. We first calculate $\langle N\rangle$ and $\langle N\rangle$ via discrete integration of equations (14) and (15). Identifying electron density samples as N_{ij}, with i the time index and j the altitude index, we form the following discrete estimates:

$$\widetilde{\langle N\rangle}_{ij} = \left[\frac{1}{M+1}\sum_{k=-M/2}^{M/2} N_{i+k,j}^2\right]^{\frac{1}{2}} \tag{17}$$

$$\langle N\rangle_{ij} = \frac{1}{M+1}\sum_{k=-M/2}^{M/2} N_{i+k,j} \tag{18}$$

where $M = T/\Delta t$ with $t = 1.2$ s and $T = 36$ s. We then substitute N, $\langle N\rangle$, and $\langle N\rangle$ into equations (10) and (11) and perform a discrete integration in altitude to estimate $\langle\Sigma\rangle$ (the average conductance over the 36 s moving window), and $\langle\Sigma\rangle$, (the corresponding photometrically derived conductance over the same window). The results are plotted in Figures 2c and 2d for Σ_H and Σ_P, respectively.

[22] Although both $\langle\Sigma\rangle$ and $\widetilde{\langle\Sigma\rangle}$ misrepresent the true conductance Σ, the significance of each effect is unique. The difference between the Σ and $\langle\Sigma\rangle$ arises from filtering of small-scale variability within the 36 s sampling window. The relative error, $(\langle\Sigma\rangle - \Sigma)/\Sigma$, is plotted in Figure 2e for Σ_H (red) and Σ_P (blue). Although this error can exceed 150% for Hall and 100% for Pedersen (factors of 2.5 and 2, respectively), the significance of the discrepancy depends on the physics being addressed. For example, the spatial-temporal scale of the excursion near 0228:10 UT may not be relevant to the closure of large-scale magnetospheric currents, but may be highly relevant to electrodynamic models of discrete arc formation.

[23] The difference between $\langle\Sigma\rangle$ and $\widetilde{\langle\Sigma\rangle}$, on the other hand, represents the systematic bias resulting from the discrepancy between $\langle N\rangle$ and $\widetilde{\langle N\rangle}$. Figure 2f gives the relative error introduced by this effect for Σ_H (red) and Σ_P (blue). As before, the magnitude of the error depends on where the sensor integration period lies with respect to the auroral activity. The average error is ~15% for Hall and ~10% for Pedersen, but can reach ~40% for Hall and ~20% for Pedersen during active periods (near 02:28 UT).

6. Discussion

[24] The satellite-based photometric measurements from which global maps of ionospheric conductance are derived represent averages over many small-scale filamentary structures. The physical information lost through temporal averaging is quantified in Figure 2e. This filtering effect has implications for the proper use of satellite-based photometry in studying MI coupling, but will not be the focus of the discussion to follow. We focus, instead, on the error introduced by the interplay between the sensor resolution and the continuity equation, quantified in Figure 2f, which is somewhat less intuitive, and can be addressed quantitatively using ground-based measurements.

6.1. Relation Between Bias and Statistical Variance

[25] Provided N is uniformly distributed within the sampling interval, the variance of N can be expressed in terms of equations (17) and (18):

$$\mathrm{Var}(N) = \widetilde{\langle N\rangle}^2 - \langle N\rangle^2. \tag{19}$$

This relationship holds whether variance is calculated over the spatial or temporal dimensions. Assuming the mobilities in equations (6) and (7) are stationary, N can be replaced with σ_H or σ_P in equation (19). Rearranging terms gives an expression for the true average conductivity $\langle\sigma\rangle$ in terms of the photometrically derived estimate $\langle\sigma\rangle$ and the variance of N:

$$\langle\sigma_H\rangle = \sqrt{\widetilde{\langle\sigma_H\rangle}^2 - [e^2(k_{He} - k_{Hi})]^2\mathrm{Var}(N)}$$

$$\langle\sigma_P\rangle = \sqrt{\widetilde{\langle\sigma_P\rangle}^2 - [e^2(k_{Pe} + k_{Pi})]^2\mathrm{Var}(N)}. \tag{20}$$

[26] Within our model assumptions, equation (20) are exact, but they do not offer a practical means of correcting $\langle\sigma\rangle$ since the instantaneous distribution of N over the sampling window cannot be measured. Since we are ultimately interested in estimating height-integrated conductivity Σ, a more useful tool is a means of correcting $\langle\Sigma\rangle$ from a proxy for $\mathrm{Var}(N)$ derived, preferably, from a higher-resolution ground-based measurement. We will consider two possible measurements: maximum E region electron density (as measured by IS radar) and ground-based luminosity (as measured by photometer or intensified camera).

6.2. Correction Using Maximum Electron Density

[27] The maximum E region density, and the altitude at which it occurs, can be routinely monitored with an IS radar at a reasonably high sample rate (.8 Hz for our Barker-coded data, ~.2 Hz for a more typical alternating code). The utility of this measurement for correcting conductance estimates

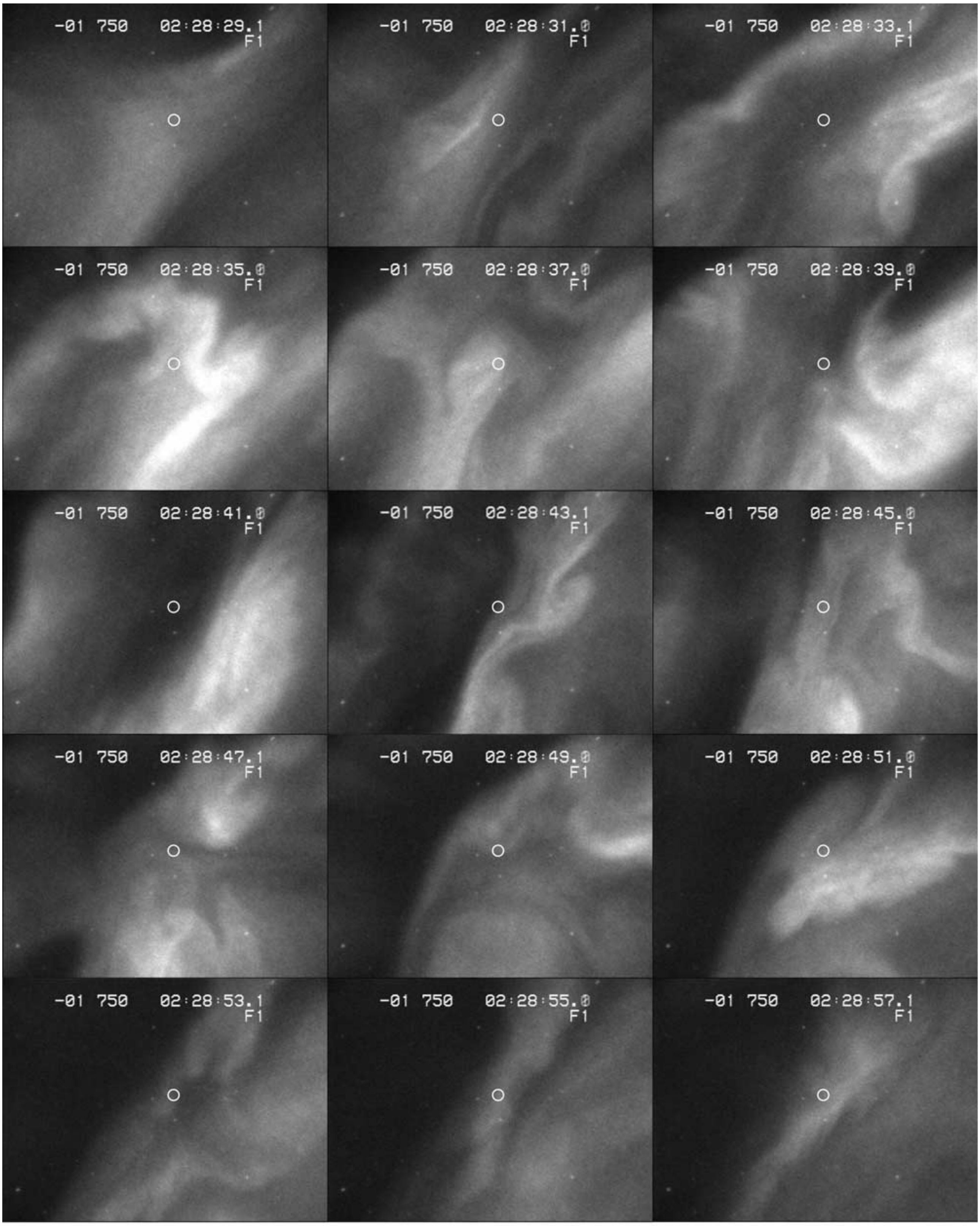

Figure 3. Sample images recorded by the narrow-field, long wavelength (>645-nm), camera during Event 2 of Figure 2. The field of view is 21 × 26 km at 100 km altitude. The spot size of the IS radar beam is indicated by the circle, and universal time is shown at the top.

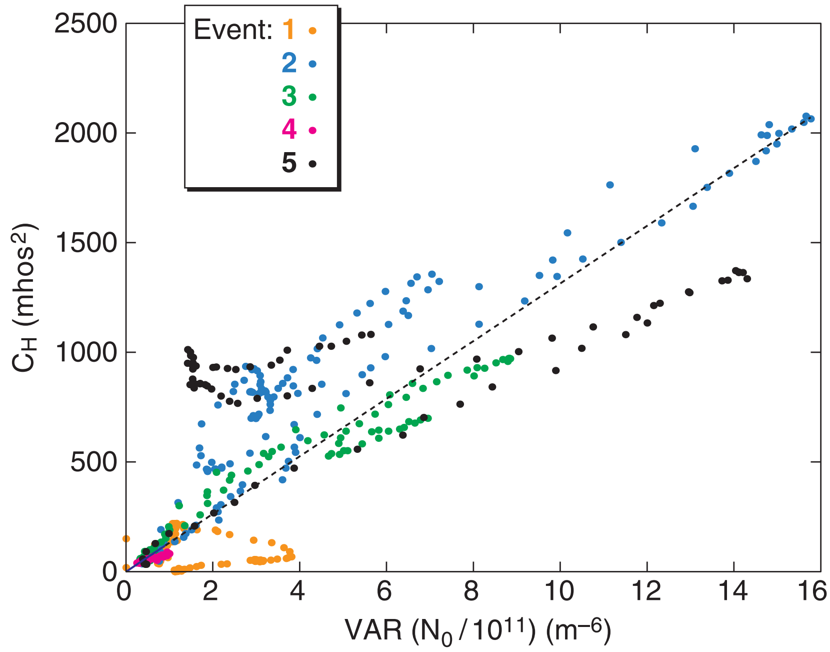

Figure 4. Variance of peak electron density, N_0, versus the correction factor for Hall conductance, C_H (from equation (22)), for each of the five color-coded events specified in Figure 2.

can be justified by considering a zero-order approximation of the integrals in equations (10) and (11),

$$\Sigma_H = e^2 (k_{He0} - k_{Hi0}) N_0 \Delta z$$

$$\Sigma_P = e^2 (k_{Pe0} + k_{Pi0}) N_0 \Delta z, \qquad (21)$$

where N_0 is the maximum density, Δz is the characteristic layer thickness, and the mobilities are evaluated at the altitude of the density maximum. Substitution into equation (19) leads to a relationship between the true average and the UV-estimated average, analogous to equation (20),

$$\langle \Sigma_H \rangle = \sqrt{\widetilde{\langle \Sigma_H \rangle}^2 - C_H}$$

$$\langle \Sigma_P \rangle = \sqrt{\widetilde{\langle \Sigma_P \rangle}^2 - C_P}, \qquad (22)$$

with variance-based correction terms

$$C_H = \left[e^2 (k_{He0} - k_{Hi0}) \Delta z \right]^2 \mathrm{Var}(N_0)$$

$$C_P = \left[e^2 (k_{Pe0} + k_{Pi0}) \Delta z \right]^2 \mathrm{Var}(N_0). \qquad (23)$$

Taking the maximum values from Figure 1 of $(k_{Pe} + k_{Pi}) = .6 \times 10^{23}$ s/kg and $(k_{He} - k_{Hi}) = 1.3 \times 10^{23}$ s/kg, and assuming $\Delta z = 30$ km, yields the following approximate expressions.

$$C_H \approx 100 \ \mathrm{Var}\left(N_0/10^{11}\right),$$

$$C_P \approx 21 \ \mathrm{Var}\left(N_0/10^{11}\right). \qquad (24)$$

where N_0 is in units of m^{-3}.

[28] In general, however, it is clear that C_H and C_P are not linear functions of Var(N_0), but depend also on the assumed layer altitude through k_e, k_i, and α. In other words, the magnitude of C_H and C_P depend not only on the variability of the auroral source, but also on the penetration depth (and, hence, characteristic energy) of the incident electrons.

[29] Rather than further treat these issues theoretically, we evaluated the efficacy of a correction scheme based on Var(N_0) directly from the experimental data of Figure 2 as follows. From the calculated values of $\langle \Sigma \rangle$ and $\widetilde{\langle \Sigma_H \rangle}$ in Figures 2c and 2d we calculated C_H and C_P directly from equation (22). We then determined N_0 for each profile and calculated its variance over a 36 s sliding window. These results are shown in Figures 4 and 5; the color coding corresponds to the five color-coded events identified in Figure 2a.

[30] In order for our statistical analysis to be self consistent, we must have no correction when the aurora is stationary, i.e., $C_H = C_P = 0$ when Var(N_0) = 0. Statistical uncertainties will cause this condition to be violated. In Figures 4 and 5 we have subtracted a bias from Var(N_0) to force this self-consistency requirement. This step is justified if we assume the uncertainty in N is caused by additive uncorrelated noise [e.g., *Papoulis*, 1965] – a reasonable model for our IS radar measurements.

[31] As anticipated, the proportionality between C and Var(N_0) in Figures 4 and 5 depends on the nature of the event in question. Event 1, for example, is concentrated above 110 km where Hall conductance is minimal. The magnitude of C_H is small regardless of Var(N_0), indicating that $\langle \Sigma_H \rangle$ represents an accurate estimate of $\widetilde{\langle \Sigma_H \rangle}$ for this event. By comparison, C_P for Event 1 shows a high sensitivity to Var(N_0). This is a manifestation of the steep gradient in $(k_{Pe} + k_{Pi})$ near 120 km in Figure 1.

[32] The other, higher-energy events show a fairly linear relationship in both C_H and C_P versus Var(N_0). The stron-

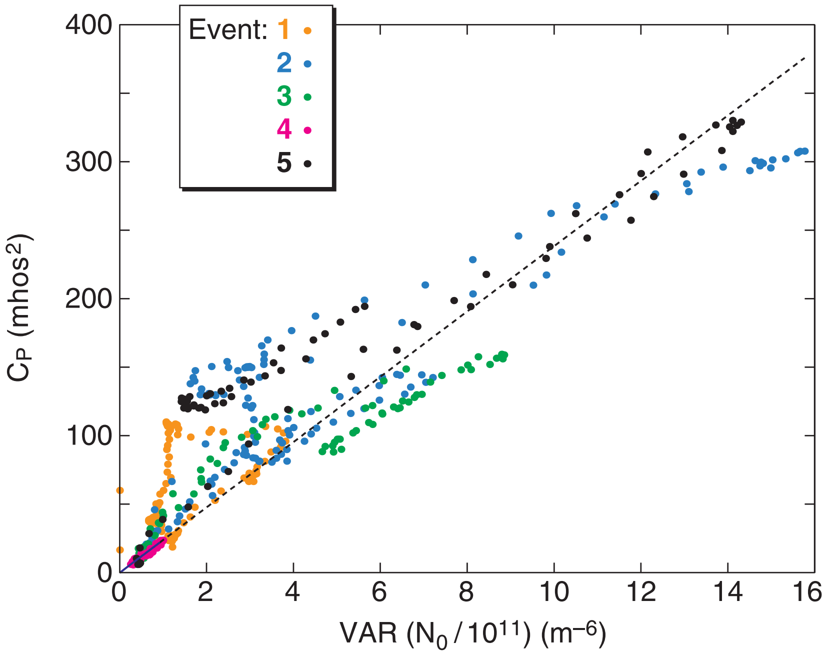

Figure 5. Same as Figure 4, but for the Pedersen correction term, C_P.

gest and most variable of these, Event 2, shows a somewhat steeper slope in C_H versus Var(N_0) than events 3 or 5. The slope of C_P versus Var(N_0) is somewhat less event dependent by comparison.

[33] The dashed lines in Figures 4 and 5 give a first-order linear least squares fit to the entire ensemble of data points and have the following functional forms:

$$C_H = 131\ \mathrm{Var}\left(N_0/10^{11}\right)$$

$$C_P = 24\ \mathrm{Var}\left(N_0/10^{11}\right) \tag{25}$$

with N_0 in units of m^{-3}. The coefficients are consistent with the approximations of equation (24). Equation (25) can be used as a first order correction on $\langle\Sigma_H\rangle$ and $\langle\Sigma_P\rangle$ in equation (22) if an estimate of Var(N_0) is available. These equations can also be interpreted as empirical estimates of equation (23).

[34] Note that, in general, optical estimates of Pedersen conductance are less sensitive to E region variability than Hall conductance, as indicated by the factor 5 difference between the coefficients. This, in turn, suggests that space-based imagers can serve as a reliable diagnostic for Joule heating studies, despite the sampling effects discussed herein.

6.3. Correction Using Auroral Luminosity

[35] A more convenient diagnostic for addressing uncertainties in space-based estimates would come from a ground-based auroral camera. The intensified camera used in this experiment has an E region field of view of 21 × 26 km, consistent with a typical E region projection for a single Polar UVI pixel. This camera, along with its edge filter, can specify the subpixel variability in ϵ_L at very high time and spatial resolution.

[36] To quantify how this measurement can be used to correct $\langle\Sigma_H\rangle$ and $\langle\Sigma_P\rangle$, we derived an expression for C_H and C_P in terms of ϵ_L, where ϵ_L now represents any optical measurement of the aurora where equation (2) holds. Applying a zero-order approximation to the integral equation (12):

$$\epsilon_L = K\alpha_0 N_0^2 \Delta z, \tag{26}$$

where the recombination coefficient α_0 is evaluated at the altitude of maximum density. Solving for N_0 and substituting into equation (23) gives expressions for C_H and C_P in terms of ϵ_L:

$$C_H = \left[e^2(k_{He0} - k_{Hi0})\right]^2 \frac{\Delta z}{K\alpha_0} \mathrm{Var}(\sqrt{\epsilon_L})$$

$$C_P = \left[e^2(k_{Pe0} + k_{Pi0})\right]^2 \frac{\Delta z}{K\alpha_0} \mathrm{Var}(\sqrt{\epsilon_L}) \tag{27}$$

The appropriate variance is, thus, over the square root of the luminosity – another consequence of the continuity equation.

[37] Following the same procedure as section 6.2, Figures 6 and 7 plot C_H and C_P versus $\mathrm{Var}\left(\sqrt{\epsilon_L}\right)$ for the two events where optical data were available. The most notable feature is the clear nonlinear trend; both C_H and C_P appear to approach an asymptotic value as the variance increases. This effect indicates a physical violation of the steady state approximation – E region plasma density cannot respond to a highly variable auroral source. As such, there is an upper limit to the variance-induced discrepancy between $\langle\Sigma_H\rangle$ and $\langle\Sigma_H\rangle$. This effect can also be clearly seen in the time domain. Figure 8 shows an enlargement of Event 2 from Figure 2b, which compared

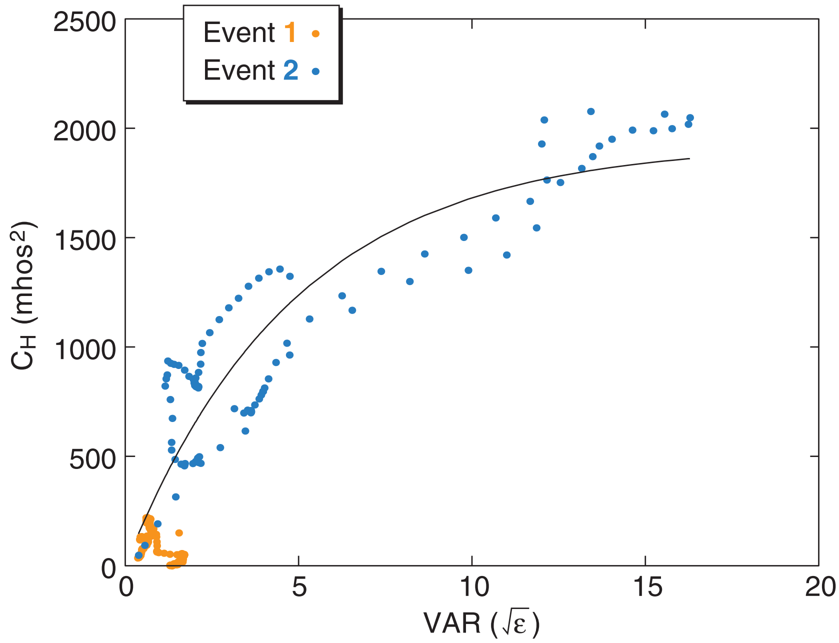

Figure 6. Variance of $\sqrt{\epsilon_L}$ versus correction factor C_H in equation (22) for the first two events specified in Figure 2.

luminosity with height-integrated production rate under a steady state assumption. Although there is good agreement when production is changing slowly (after 02:29 UT), the *E* region response lags the optical curve during periods of high variability.

[38] Thus, during active periods luminosity becomes a poor proxy for conductivity, regardless of the sampling resolution. This is an important consideration when interpreting ephemeral auroral luminosity; for the purposes of this study, this ionospheric filter impacts the manner in which ground-based photometry would be used in correcting our satellite-based conductance estimate. In particular, C_H and C_P cannot be parameterized by linear functions of $\mathrm{Var}\sqrt{\epsilon_L}$. The solid lines in Figures 6 and 7 give a least squares fit with the following functional forms:

$$C_H = 1930[1 - \exp(-.20\ \mathrm{Var}(\sqrt{\epsilon_L}))]$$

$$C_P = 300[1 - \exp(-.21\ \mathrm{Var}(\sqrt{\epsilon_L}))]. \qquad (28)$$

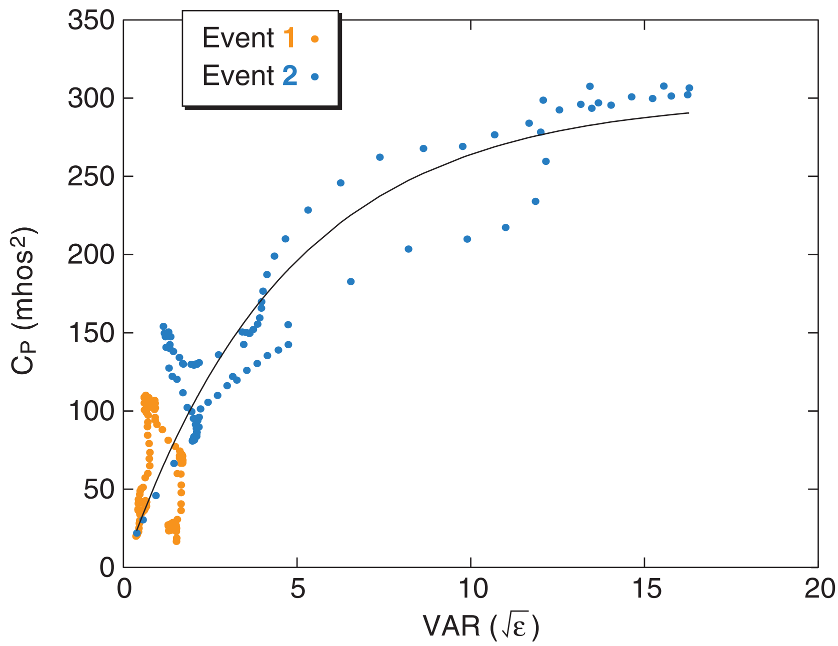

Figure 7. Same as Figure 6, but for C_P.

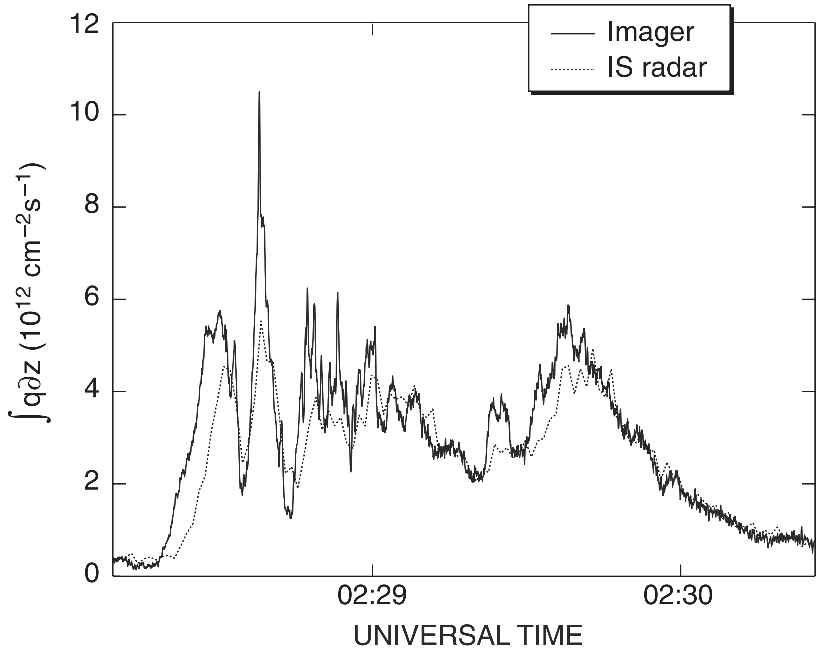

Figure 8. Detail of the 02:28 to 02:29 interval of Figure 2b, showing the lag between the true production rate (detected optically) and the production rate estimated through height integration of equation (5).

Unlike equation (25), the coefficients of equation (28) are only relevant to this particular optical sensor since the data have not been calibrated to energy flux.

7. Summary and Concluding Remarks

[39] We have described a fundamental systematic error introduced whenever photometric measurements of the aurora are used with a theoretical calculation of ion production to estimate conductivity. This has been the approach of numerous studies [*Vickrey et al.*, 1981; *Wallis and Budzinski*, 1981; *Spiro et al.*, 1982; *Germany et al.*, 1994], which are generally based on the energy deposition calculations of *Rees* [1963]. The magnitude of the error depends on the variance of the aurorally produced electron density as described by equation (20). The effect is the same whether the variance is over space or time. We have also quantified the information lost as a result of undersampling auroral variability – a problem inherent to all space-based imaging systems.

[40] Uncertainties in photometrically derived ionospheric density and conductance are typically discussed within the context of three types of errors: (1) photometric calibration (2) geographic registration, and (3) model assumptions imposed in the analysis. The sampling effects discussed herein are of a rather different nature and, to our knowledge, have not yet been treated formally.

[41] We have proposed two approaches to addressing these errors using ancillary diagnostic measurements. Of particular utility is the correction using ground-based optics expressed by equations (22), (27), and (28), and Figures 6 and 7, as it allows both the spatial and temporal variance to be quantified. Such a correction can only be applied to a very limited number of pixels in a satellite image sequence. But the results would be, nonetheless, valuable in understanding the impact of small-scale structuring on global estimates of conductance.

[42] These issues are of particular relevance because of the proliferation of auroral imaging systems on satellites, and the application of these measurements to magnetosphere–ionosphere coupling. A reliable estimate of the global distribution of ionospheric conductance is crucial for data assimilation techniques such as AMIE (Assimilated Mapping of Ionospheric Electrodynamics) [*Richmond and Kamide*, 1988]. Space-based imaging spectrometers can contribute greatly to this problem, but it is crucial that measurement effects and physical assumptions be properly understood before the results are used in a scientific context.

[43] **Acknowledgments.** This work has benefited from many valuable discussions with Craig Heinselman and Jeffrey Thayer. We also gratefully acknowledge Mary McCready for processing the radar data, the Sondrestrom crew for campaign support, and Werner Lieb of the Max Planck Institute for his role in developing the optical instrumentation. This research was supported by NSF grants ATM-9813556 and ATM-0001899.

[44] Lou-Chuang Lee and Chin S. Lin thank the two reviewers for their assistance in evaluating this paper.

References

Brekke, A., *Physics of the Upper Polar Atmosphere*, pp. 231–233, John Wiley, New York, 1997.

Doe, R. A., J. D. Kelly, D. Lummerzheim, G. K. Parks, M. J. Brittnacher, G. A. Germany, and J. Spann, Initial comparison of Polar UVI and Sondrestrom IS radar estimates for auroral electron energy flux, *Geophys. Res. Lett.*, *24*(8), 999–1002, 1997.

Germany, G. A., D. G. Torr, P. G. Richards, M. R. Torr, and S. John, Determination of ionospheric conductivities from FUV auroral emissions, *J. Geophys. Res.*, *99*(A12), 23,297–23,305, 1994.

Kamide, Y., A. D. Richmond, and S. Matsushita, Estimation of ionospheric electric fields, ionospheric currents, and field-aligned currents from ground magnetic records, *J. Geophys. Res.*, *86*(A2), 801–813, 1981.

Lummerzheim, D., and J. Lilensten, Electron transport and energy degradation in the ionosphere: Evaluation of the numerical solution, comparison with laboratory experiments and auroral observations, *Ann. Geophys.*, *12*, 1039–1051, 1994.

Papoulis, A., *Probability, Random Variables, and Stochastic Processes*, 583 pp., McGraw-Hill, New York, 1965.

Rees, M. H., Auroral ionization and excitation by incident energetic electrons, *Planet Space Sci.*, *11*, 1209–1218, 1963.

Rees, M. H., and D. Luckey, Auroral electron energy derived from ratio of spectroscopic emissions, 1, Model computations, *J. Geophys. Res.*, *79*(34), 5181–5186, 1974.

Richmond, A. D., and Y. Kamide, Mapping electrodynamic features of the high-latitude ionosphere from localized observations: Technique, *J. Geophys. Res.*, *93*(A6), 5741–5759, 1988.

Rishbeth, H., and O. K. Garriott, *Introduction to Ionospheric Physics*, *Int. Geophys. Ser.*, vol. 14, pp. 132–142, Academic, San Diego, Calif., 1969.

Semeter, J., D. Lummerzheim, and G. Haerendel, Simultaneous multi-spectral imaging of the discrete aurora, *J. Atmos. Sol. Terr. Phys.*, *63*, 1981–1992, 2001.

Spiro, R. W., P. H. Reiff, and L. J. Maher Jr., Precipitating electron energy flux and auroral zone conductances: An empirical model, *J. Geophys. Res.*, *87*(A10), 8215–8227, 1982.

Strickland, D. J., R. R. Meier, J. Hecht, and A. B. Christensen, Deducing composition and incident electron spectra from ground-based auroral optical measurements: Theory and modeling results, *J. Geophys. Res.*, *94*(A10), 13,527–13,539, 1989.

Torr, M. R., et al., A far ultraviolet imager for the international solar-terrestrial physics mission, *Space Sci. Rev.*, *71*, 329–383, 1995.

Vickrey, J. F., R. R. Vondrak, and S. J. Matthews, The diurnal and latitudinal variation of auroral zone ionospheric conductivity, *J. Geophys. Res.*, *86*(A1), 65–75, 1981.

Vickrey, J. F., R. R. Vondrak, and S. J. Matthews, Energy deposition by precipitating particles and joule dissipation in the auroral ionosphere, *J. Geophys. Res.*, *87*(A7), 5184–5196, 1982.

Wallis, D. D., and E. E. Budzinski, Empirical models of height integrated conductivities, *J. Geophys. Res.*, *86*(A1), 125–137, 1981.

R. Doe and J. Semeter, SRI International, 333 Ravenswood Avenue, Menlo Park, CA 94025, USA. (Richard.Doe@sri.com; Joshua.Semeter@sri.com)